

# The Role of Phosphorous in the Solid Electrolyte Interphase of Argyrodite Solid Electrolytes

Matthew Burton<sup>1,2</sup>, Ben Jagger<sup>1</sup>, Yi Liang<sup>1</sup>, Joshua S. Gibson<sup>1</sup>, Jack Aspinall<sup>1</sup>, Jack E. N. Swallow<sup>1</sup>, Robert S. Weatherup<sup>1,3</sup>, and Mauro Pasta<sup>1,2</sup>

<sup>1</sup>Department of Materials, University of Oxford, Parks Road, Oxford OX1 3PH, United Kingdom

<sup>2</sup>The Faraday Institution, Quad One, Harwell Science and Innovation Campus, Didcot OX11 0RA, United Kingdom

<sup>3</sup>Diamond Light Source, Harwell Science and Innovation Campus, Didcot OX11 0DE, United Kingdom

\* Corresponding author:

mauro.pasta@materials.ox.ac.uk

## Context & Scale

All-solid-state lithium metal batteries are a promising emerging technology that could offer higher energy density, faster charging, and improved safety compared to Li-ion batteries. Argyrodite-type solid electrolytes (SEs) are considered the most promising candidates to enable this technology due to their high ionic conductivities and perceived kinetic stability in contact with the lithium metal anode. However, recent studies have shown that the solid electrolyte interphase (SEI) between argyrodite and the anode grows continually via a diffusion-controlled mechanism, with detrimental implications for cell impedance and electrolyte consumption. This work reveals the role of phosphorus in the mechanism behind this continual growth, opening the door for researchers to explore potential solutions.

## Summary

The solid electrolyte interphase that forms on  $\text{Li}_6\text{PS}_5\text{Cl}$  argyrodite solid electrolytes has been reported to continually grow through a diffusion-controlled process, yet this process is not fully understood. Here, we use a combination of electrochemical and X-ray photoelectron spectroscopy techniques to elucidate the role of phosphorus in this growth mechanism. We uncover how  $\text{Li}_6\text{PS}_5\text{Cl}$  can decompose at potentials well above the full reduction to  $\text{Li}_3\text{P}$ , forming partially lithiated phosphorus species  $\text{Li}_x\text{P}$ . We provide evidence of a gradient of  $\text{Li}_x\text{P}$  species throughout the SEI thickness, consistent with diffusion-limited growth. We predict continuous SEI growth as long as lithium metal is present, necessitating the need to develop surface engineering approaches.

## Introduction

The transition from fossil fuels is leading to an ever-growing demand for batteries.<sup>1</sup> One such demand is transportation, where increased energy density is required for improved range. Lithium metal anode batteries hold promise in this area by significantly increasing the specific capacity of the anode with the highest energy density achieved in a zero-lithium excess configuration.<sup>2</sup> Dendritic growth

of lithium during charging results in cell lifetime and safety issues when used with a liquid electrolyte.<sup>3</sup> In theory, this issue can be overcome with a solid electrolyte (SE), that should possess the mechanical strength to suppress the dendritic growth.<sup>4</sup>

Several Li-ion conducting solid electrolytes have been discovered.<sup>5</sup> Oxides possess the lowest theoretical reduction potentials and thus greatest stability against Li metal anodes,<sup>6</sup> however, to date their ionic conductivities have proven to be too

low for practical applications.<sup>5</sup> In contrast, sulfides have exhibited ionic conductivities in excess of those shown by liquid electrolytes.<sup>5</sup> The most promising of the sulfide solid electrolytes are the argyrodites (which have a chemical composition of or near  $\text{Li}_6\text{PS}_5\text{Cl}$ ), due to their greater stability compared to other sulfides.<sup>7</sup>

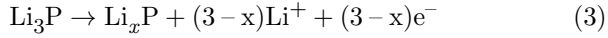
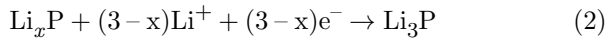
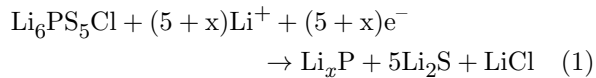
The theoretical reduction potential of  $\text{Li}_6\text{PS}_5\text{Cl}$  is 1.71 V vs.  $\text{Li}^+/\text{Li}$ ,<sup>6</sup> so Li should react with  $\text{Li}_6\text{PS}_5\text{Cl}$  to form an interphase. This reactively formed interphase could be a mixed conducting interphase (MCI) or a metastable solid electrolyte interphase (SEI).<sup>8</sup> If the interphase that forms is ionically conductive, electrically resistive and chemically stable against both Li and the SE, then it will form an SEI passivation layer that prevents any further degradation of SE and loss of Li.<sup>9</sup> The thickness, properties and composition of the SEI however are poorly understood. Thickness estimates of the SEI have ranged from a few nm to several hundred,<sup>10,11</sup> with compositions that have been seen to vary with operating conditions.<sup>12</sup> Recent work by the Janek group has shown that the SEI may continually grow through an unknown diffusion process.<sup>13</sup> If the SEI is too ionically resistive, then the additional overpotential requirements for a thick SEI would lead to cell failure.<sup>14</sup> Additionally, if the SEI is not fully dense it may cause the initiation of cracks leading to cell shorting.<sup>15</sup> It is imperative, therefore, that the SEI must be better understood.

This work investigates the mechanism behind the continual growth of Li-argyrodite SEI, tying behaviour to the SEI composition. The electrochemical stability of the SEI is probed through cyclic voltammetry (CV), whilst its conductivity through a combination of coulometric titration time analysis (CTTA) and three electrode potentiostatic electrochemical impedance spectroscopy (PEIS). The evolution of the SEI's chemical composition is measured through virtual electrode plating X-ray photoemission spectroscopy (VEP-XPS), whilst non-destructive depth profiling of the SEI is performed using soft and hard X-ray photoelectron spectroscopy (SOXPES and HAXPES).

## Results and Discussion

The reduction potential of  $\text{Li}_6\text{PS}_5\text{Cl}$  was assessed using cyclic voltammetry (CV) with a planar stainless steel electrode setup (Figure 1a). Stainless steel does not alloy with lithium and exhibits negligible lithium

diffusivity compared to other current collector materials.<sup>13</sup> During the first reductive sweep, two clear peaks can be observed (labelled *a* and *b* in Figure 1a). Peak *a* can be ascribed to the reduction of argyrodite to form partially lithiated phosphorous species ( $\text{Li}_x\text{P}$ , Equation 1) and has an onset potential of 1.13 V vs.  $\text{Li}^+/\text{Li}$ , below the computationally predicted value of 1.71 V vs.  $\text{Li}^+/\text{Li}$ ,<sup>6</sup> yet significantly higher than previously thought.<sup>16</sup> While S and Cl thermodynamically should be fully reduced upon the reduction of the electrolyte to form  $\text{Li}_2\text{S}$  and  $\text{LiCl}$  respectively, P should not.<sup>6</sup> Instead, P could exist as a number of different partially lithiated states, which can be summarised as  $\text{Li}_x\text{P}$  (where  $x < 3$ ). Peak *b* can be attributed to the reduction of the partially lithiated  $\text{Li}_x\text{P}$  to form the fully reduced  $\text{Li}_3\text{P}$  (Equation 2). During the oxidative sweep, a peak can be seen (labelled *c*) at 0.87 V vs.  $\text{Li}^+/\text{Li}$ . The potential is too low for the oxidation of  $\text{Li}_6\text{PS}_5\text{Cl}$ ,  $\text{Li}_2\text{S}$  or  $\text{LiCl}$  (Figure S1), however, is in line with the reoxidation of  $\text{Li}_3\text{P}$  to  $\text{Li}_x\text{P}$  (Equation 3).<sup>6,17,18</sup>



On subsequent cycles (Figure 1b) peak *a* is no longer clearly visible suggesting that most of the SEI growth occurs on the first reductive sweep. Nonetheless, a clear increase in the peak current of peak *c* with cycling is indicative of a continuous growth of the SEI.

To gain further insight into SEI growth, we performed a modified version of CTTA (Figure 2a), previously reported by the Janek group.<sup>13</sup> Our results show a similar rate of Li consumption (Figure 2b). We included an additional PEIS step between lithium plating cycles, using a novel 3-electrode setup with an In+25% Li ring reference electrode,<sup>19</sup> specifically designed to minimize impedance artifacts (Figure 2b, insert).

CTTA electroplates a set amount of lithium through the SE onto the current collector, then waits

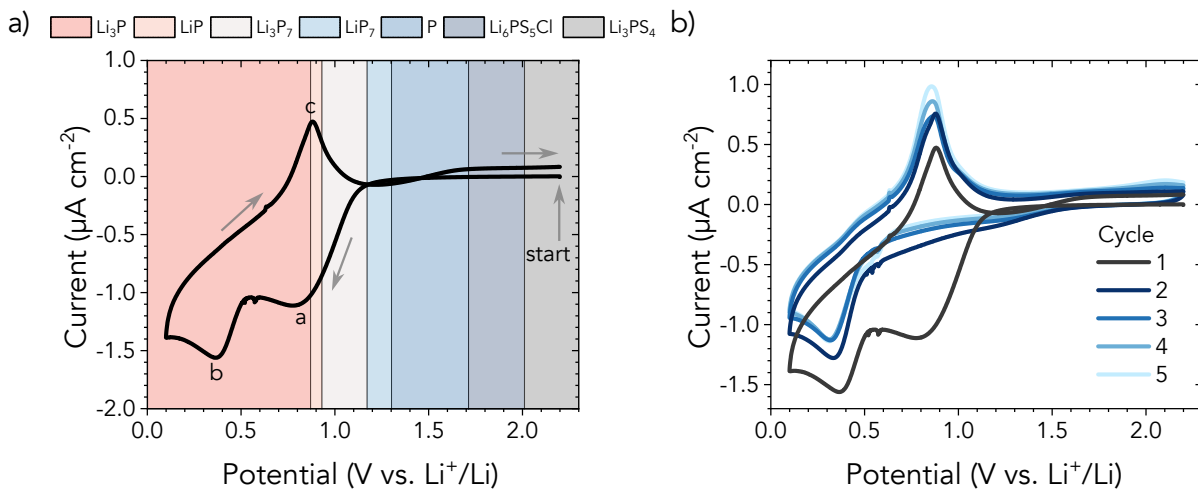


Figure 1: Cyclic voltammetry at 13 MPa of  $\text{Li}_6\text{PS}_5\text{Cl}$  with a Li counter electrode and a stainless steel working/blocking electrode. a) CV at  $100 \mu\text{V s}^{-1}$  and a starting potential of 2.2 V vs.  $\text{Li}^+/\text{Li}$  of  $\text{Li}_6\text{PS}_5\text{Cl}$  (background coloring representing theoretical phosphorus thermodynamic stability windows),<sup>6</sup> b) several CVs cycles.

for all the lithium to be consumed by SEI formation before repeating the cycle. The impedance (sinus amplitude 10 mV, 400 kHz to 10 Hz) was measured when all the plated lithium had been consumed, i.e., when the 50 mV vs.  $\text{Li}^+/\text{Li}$  cutoff was reached, but before the subsequent lithium plating step (Figure 2a).

The SEI impedance can be fitted to a simple Randles circuit, with the semi-infinite Warburg impedance replaced with a finite diffusion with a reflective boundary (Figure 2c, insert). This fit is equivalent to previous SEI fits,<sup>12,20,21</sup> except the finite diffusion transmission line for the SEI is more representative of the multi-component nature of the SEI.<sup>22</sup> The reflective boundary is due to the finite thickness of the SEI, and the electrode being above the Li plating potential. In total 32 plating steps of  $1.56 \mu\text{A h cm}^{-2}$  each were performed.

The resistance from the finite diffusion ( $R_{\text{SEI}}$ ), can be seen to progressively increase with increasing charge passed (Figure 2d and Figure S2 for against time). The trend however, is not seen to be linear as would be expected with a SEI that grows with uniformity with respect to chemical composition and morphology, but rather curves away to a reduced resistance. Highly yet not fully lithiated  $\text{Li}_x\text{P}$  ( $x > 1.5$ ) is suggested to have a slightly higher Li ion diffusion coefficient (and thus higher ionic conductivity) than  $\text{Li}_3\text{P}$  (Figure S5),<sup>18</sup> which could explain this trend. If the initial  $20 \mu\text{A h cm}^{-2}$  of  $R_{\text{SEI}}$  is fitted linearly

through the origin, assuming negligible electronic conductivity and a fully dense SEI, which solely consists of  $\text{Li}_3\text{P}$ ,  $\text{Li}_2\text{S}$  and  $\text{LiCl}$  ( $1 \mu\text{Ah cm}^{-2} \approx 9 \text{ nm}$ )<sup>13</sup>, an ionic conductivity of  $204 (\pm 8) \text{ nS cm}^{-1}$  is yielded. This is directly comparable to the recently published ionic conductivity of a synthetic SEI of  $\text{Li}_6\text{PS}_5\text{Cl}$  ( $134 \text{ nS cm}^{-1}$ ).<sup>23</sup>

After  $\sim 1000$  hours of CTTA and  $\sim 50 \mu\text{A h cm}^{-2}$  of accumulated charge the cell was left at OCV with PEIS taken every hour for 400 hours (Figure 3a). The OCV is observed to increase over time and interestingly seems to mirror the delithiation profile of red phosphorous (Figure S6).<sup>18</sup>  $R_{\text{SEI}}$  is seen to also increase over the OCV period, indicating either SEI growth, a compositional change or a combination of both. Whilst highly lithiated  $\text{Li}_x\text{P}$  is suggested to have a higher Li diffusivity than  $\text{Li}_3\text{P}$ , the diffusivity of Li in  $\text{Li}_x\text{P}$  is suggested to decrease from a peak when  $x$  is  $\sim 2.5$  until  $x$  reaches  $\sim 0.75$  (Figure S5).<sup>18</sup> This would result in an increased ionic resistance. In addition, the delithiation of P would result in further decomposition of  $\text{Li}_6\text{PS}_5\text{Cl}$  increasing the thickness of the SEI (Equation S6).

To investigate further the cause of the changing OCV potential, VEP-XPS was performed.<sup>12</sup> Lithium ( $\sim 0.01 \text{ mAh cm}^{-2}$ ) was plated through a 5 mm  $\text{Li}_6\text{PS}_5\text{Cl}$  pellet over 1 hour using an electron beam current of  $2.5 \mu\text{A}$  ( $\sim 0.01 \text{ mA cm}^{-2}$ ), as previously reported.<sup>12</sup> XPS was then performed continuously, yielding a new data set every 53 minutes. Whilst

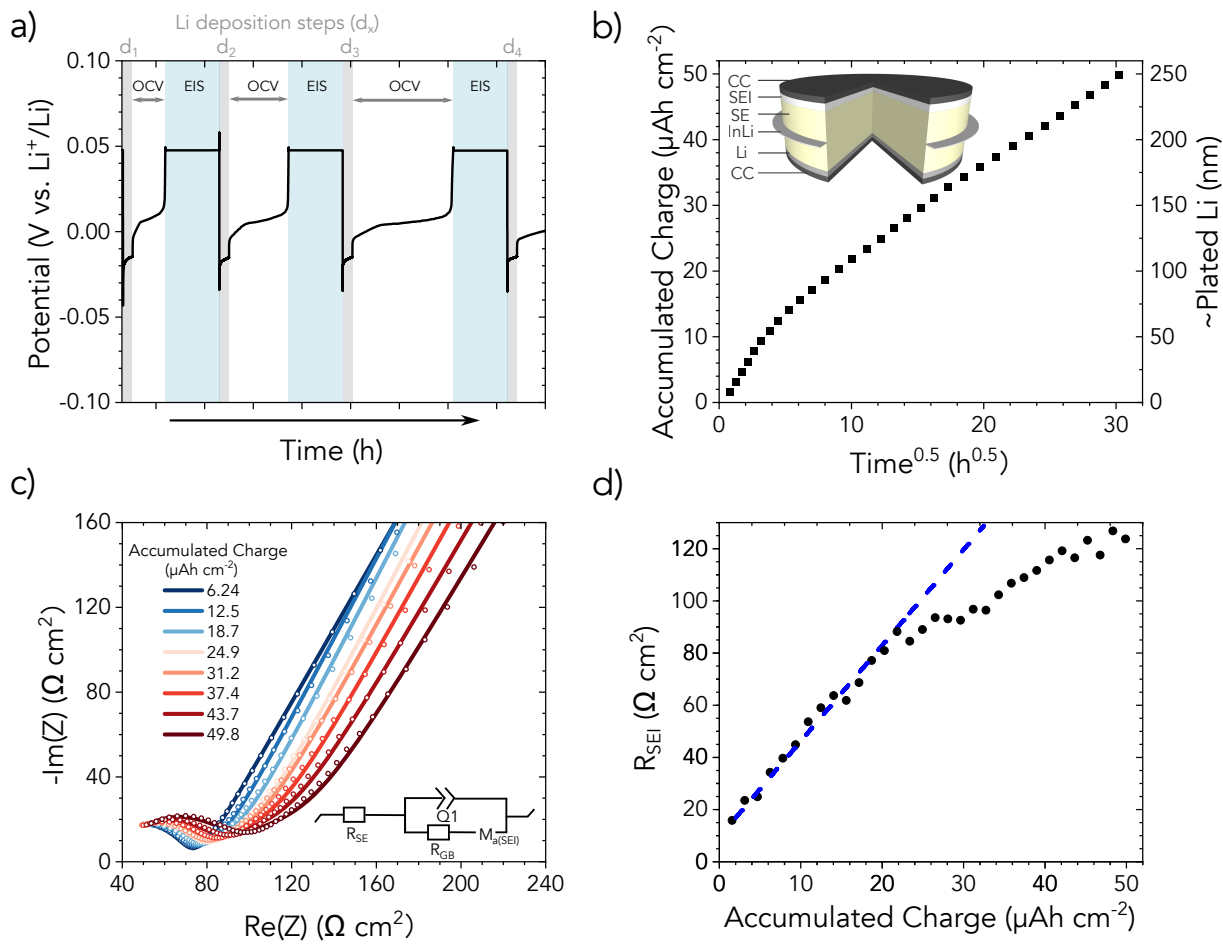


Figure 2: Three electrode CTTA measurement. a) CTTA with PEIS conducted once a 50 mV OCV was reached (see Figure S3 for real data), b) relationship between accumulated charge and the square root of OCV time to consume Li metal (insert schematic of the three electrode setup), c) PEIS of a growing SEI (circles data, lines fits) with the equivalent circuit (for details of the  $M_a$  element see Figure S4), d) calculated SEI resistance before each titration step (with the straight dotted blue line indicating the nonlinearity of the results).

$\text{Li}_2\text{S}$  is seen to remain stable (Figure S7),  $\text{Li}_3\text{P}$  is seen to evolve (Figure 3c-e). When freshly lithiated, the P spectra can be seen to consist of only  $\text{Li}_3\text{P}$  and residual  $\text{Li}_6\text{PS}_5\text{Cl}$ , while after the lithium metal is consumed  $\text{Li}_x\text{P}$  can be seen to emerge along with a decrease of the  $\text{Li}_3\text{P}$  peak. An increase in the  $\text{Li}_6\text{PS}_5\text{Cl}$  peak is also seen, which is most likely due to the emergence of an additional  $\text{Li}_x\text{P}$  species with a lower  $x$  as we also observe elemental red phosphorus in this binding energy region (Figure S8). These results prove that the SEI composition evolves through a delithiation process of phosphorous.

To further probe the composition of the SEI,

soft and hard X-ray photoelectron spectroscopy (SOXPES and HAXPES) measurements were performed. Photoelectrons emitted during SOXPES had a kinetic energy of 315 eV and HAXPES was performed with incident photon energies of 2.2 keV and 6.6 keV, resulting in electron inelastic mean free paths (IMFPs) of  $\sim 1$ ,  $\sim 5$  and  $\sim 14$  nm, respectively (Figure S9). SOXPES and HAXPES were first performed on a pristine  $\text{Li}_6\text{PS}_5\text{Cl}$  pellet (Figure S10), revealing only minor  $\text{Li}_2\text{S}$ ,  $\text{Li}_2\text{SO}_4$ ,  $\text{Li}_2\text{CO}_3$  and  $\text{LiOH}$  impurities.

SOXPES and HAXPES were then performed following the in situ evaporation of approximately

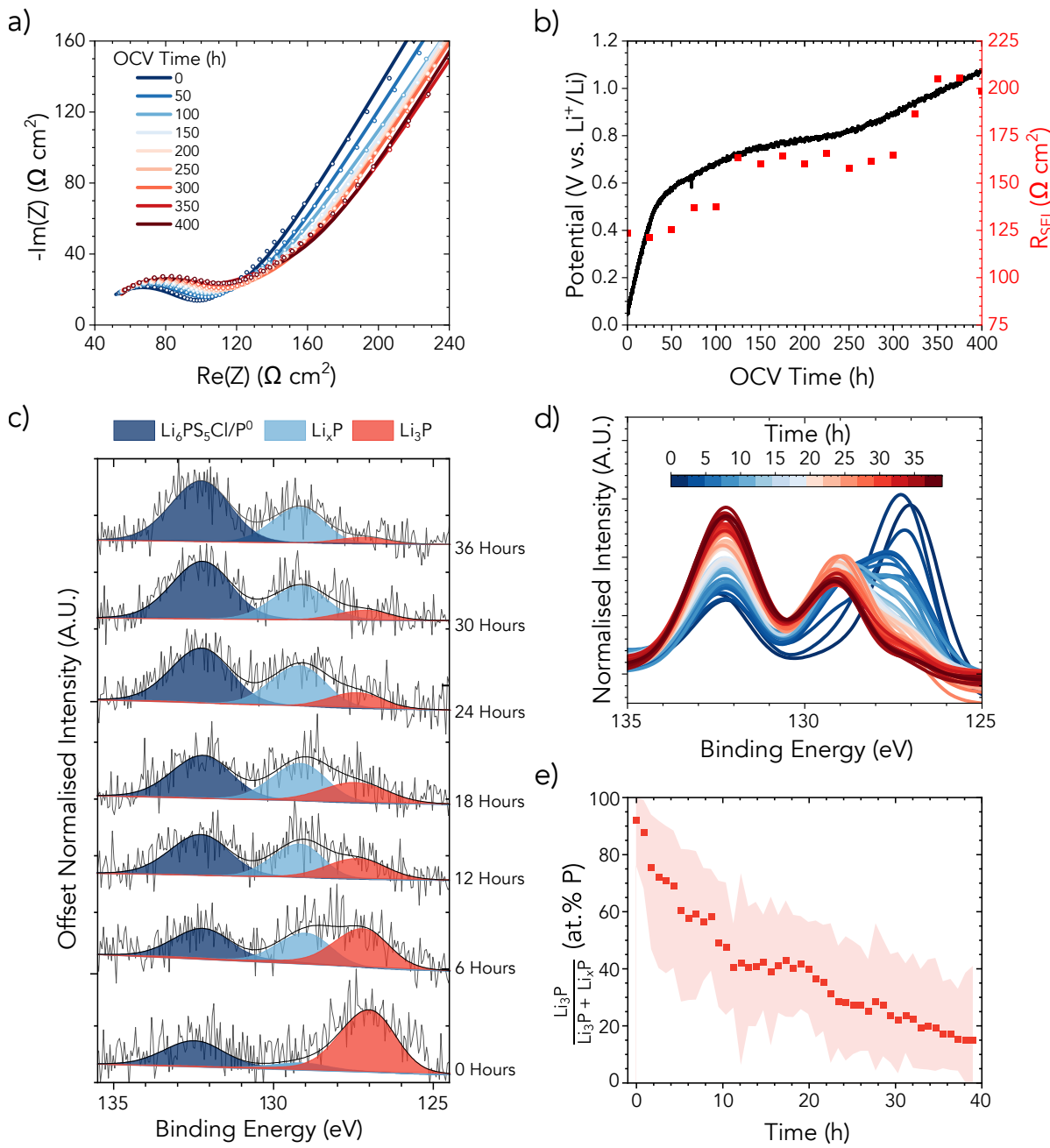


Figure 3: Evolution of the SEI. a) evolution of the SEI impedance in lithium free conditions (circles data, lines fits) following on from CTIA from Figure 2, b) evolution of OCV potential and SEI resistance in lithium free conditions. c) XPS of phosphorous in the SEI after  $\sim 0.01 \text{ mAh cm}^{-2}$  of lithium was VEP through a  $\text{Li}_6\text{PS}_5\text{Cl}$  pellet over 1 hour using an ebeam current of  $2.5 \mu\text{A}$  ( $\sim 0.01 \text{ mA cm}^{-2}$ ), d) the mean normalised phosphorous  $2p$  fitted spectrum over time, e) percentage of  $\text{Li}_3\text{P}$  in the P-containing SEI species (with the dots being the calculated value and the shaded areas the uncertainty calculated from the peak area standard deviations).

20 nm of lithium metal onto the  $\text{Li}_6\text{PS}_5\text{Cl}$  surface (denoted as 0 h) and then repeated after 6 and 12 h (Figure S11).<sup>24</sup> Figure 4a shows the fitted S 2p region where peaks attributed to both  $\text{Li}_6\text{PS}_5\text{Cl}$  and  $\text{Li}_2\text{S}$  can be observed and reliably separated. The S 2p region can therefore provide information about SEI formation and growth. At 0 h  $\text{Li}_2\text{S}$  is the dominant species in the SOXPES data, but its mole fraction decreases as the incident photon energy, and therefore probing depth, increases (Figure 4b), enabling photoelectrons to be detected from the underlying  $\text{Li}_6\text{PS}_5\text{Cl}$ . Between 0 h and 6 h the SOXPES data remains almost constant, but the proportion of  $\text{Li}_2\text{S}$  evident at 2.2 and 6.6 keV increases, indicating growth of the SEI. The SEI then grows further between 6 and 12 h, although at a reduced rate.

It is expected that the concentrations of  $\text{LiCl}$  and  $\text{Li}_x\text{P}$  will also increase in accordance with the  $\text{Li}_2\text{S}$ . However, the low concentration of P in  $\text{Li}_6\text{PS}_5\text{Cl}$ , combined with its low photoionization cross section<sup>25</sup>, unfortunately results in poorer signal-to-noise ratios for the corresponding P 2s and P 2p regions in Figure S11. Nevertheless, it is clear from the 2.2 keV P 2p region and particularly the 6.6 keV P 2s region in Figure 4c that the SEI is composed of several P-containing species. Consistent with previous reports<sup>23</sup>, these are attributed to  $\text{Li}_3\text{P}$  at the lowest binding energy and  $\text{Li}_x\text{P}$  with decreasing lithium content as the binding energy increases. Additionally, as described above, the  $\text{Li}_6\text{PS}_5\text{Cl}$  peak may overlap with elemental phosphorus. Figure 4d shows that the proportion of  $\text{Li}_3\text{P}$  in the SEI is highest at 0 h and small probing depth (2.2 keV) and this proportion reduces as both time and probing depth increase allowing thicker SEIs to be studied. This suggests a layer of  $\text{Li}_3\text{P}$  forms first close to the lithium metal and further SEI growth results in the formation of less lithiated  $\text{Li}_x\text{P}$  further away from the lithium anode, resulting in a gradient of composition through the SEI.

An additional experiment was performed to uncover how the SEI changes once the lithium metal is consumed. As evident in Figure S12, immediately after lithium evaporation a gradient of lithiated P is again formed within the SEI, with less lithiated  $\text{Li}_x\text{P}$  observed further from the Li. However, after 22 h, once the lithium metal has disappeared, the proportion of  $\text{Li}_3\text{P}$  decreases, consistent with the previous evidence that  $\text{Li}_3\text{P}$  delithiation can drive further  $\text{Li}_6\text{PS}_5\text{Cl}$  decomposition.

All the experimental evidence therefore suggest the presence of a gradient of lithiated phosphorus in the SEI. This is in agreement with a recent study by Ren et al. which computationally predicted that the SEI of  $\text{Li}_3\text{PS}_4$  contains at least two phosphorus regions.<sup>26</sup> One with a Li to P coordination number of 11 near the Li electrode corresponding to  $\text{Li}_3\text{P}$ , and another with a Li to P coordination number of 6 near the solid electrolyte corresponding to  $\text{LiP}$ .

We rationalize this observation using the mechanism depicted in Figure 4e. When fresh argyrodite is placed in contact with the stainless steel current collector in a lithium-free configuration, the potential is swept cathodically during the first charge until the lower limit of the argyrodite's electrochemical stability window is reached, triggering its decomposition into  $\text{Li}_x\text{P}$  species (Equation 1) and, at lower potentials,  $\text{Li}_3\text{P}$  (Equation 2). Lithium metal then plates onto the current collector. However, this remains a metastable state because the electrochemical potential of electrons in  $\text{Li}_x\text{P}$  is high enough to further reduce the argyrodite (Figure S1), partially delithiating  $\text{Li}_x\text{P}$  (Equation S6) and creating a lithium chemical potential gradient across the SEI. As a result, the SEI continues to grow as long as lithium metal is present to "feed" lithium through it. The previously observed diffusion-limited behavior can thus be attributed to lithium diffusion through lithiated phosphorus species. Since lithium diffusivity is composition dependent,<sup>18</sup> the SEI conductivity changes over time and space, explaining the trend observed in Figure 2d. If fresh lithium metal is directly put in contact with argyrodite, a layer of  $\text{Li}_3\text{P}$  will form first triggering a similar mechanism to the one described above.

We therefore predict a continuous SEI growth as long as lithium metal is present. When all the lithium is consumed,  $\text{Li}_3\text{P}$  will over time delithiate and the source of lithium will be exhausted.

The practical implications of this are quite impactful to the implementation of solid state batteries as the SEI impedance is predicted to continuously grow, consuming lithium and solid electrolyte and increasing the overall cell impedance. Janek has predicted the need to keep SEI resistance below  $10 \Omega \text{ cm}^{-2}$ ,<sup>23,27</sup> highlighting the importance of finding a mechanism to halt diffusion-controlled SEI growth. By understanding the diffusion mechanism behind this growth, potential routes to stop it can now be explored. We do not expect metallic

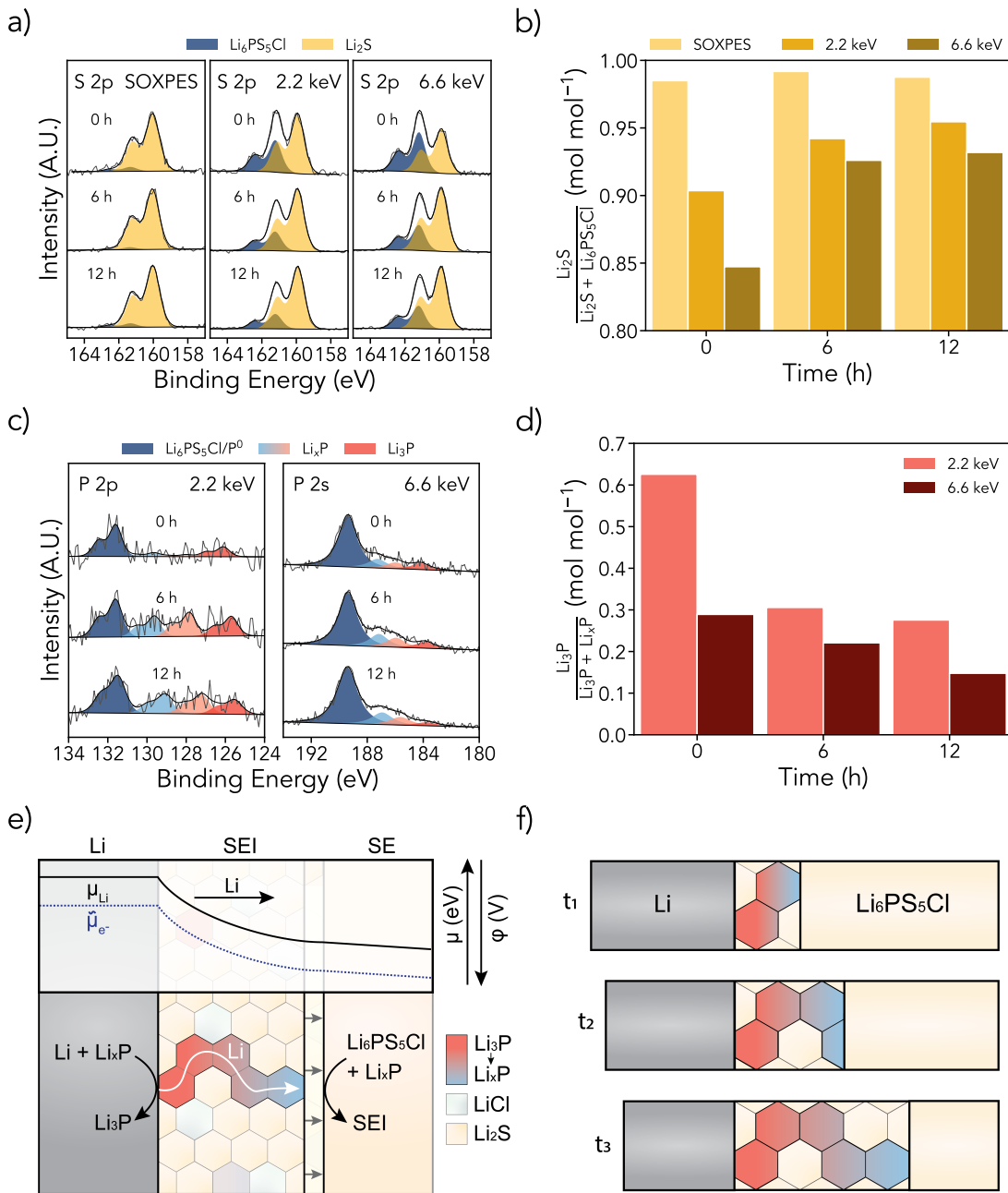


Figure 4: SOXPES and HAXPES on an  $\text{Li}_6\text{PS}_5\text{Cl}$  pellet with  $\sim 20$  nm of Li evaporated on top: a) normalized S 2p spectra gathered using SOXPES and HAXPES with time and incident X-ray energies marked on the plot. b) mole fraction of  $\text{Li}_2\text{S}$  in the S 2p region calculated from the spectra in a), demonstrating an increase in the proportion of  $\text{Li}_2\text{S}$  with decreasing probing depth and with increasing time. c) normalized P spectra gathered using SOXPES and HAXPES with time and incident X-ray energies marked on the plot. d) mole fraction of  $\text{Li}_3\text{P}$  in the P-containing SEI species calculated from the spectra in c), demonstrating a reduction in proportion of  $\text{Li}_3\text{P}$  with increasing probing depth and with increasing time. Schematic illustrations of the growing SEI: e) the chemical potential dropping over the SEI resulting in a lithium gradient in phosphorous and the resulting SEI growth reactions (further details provided in the SI), f) the SEI growth through time.

interlayers to help but electronically insulating interlayers could be introduced by introducing a steep decrease in the electrochemical potential of the electrons below the electrolyte decomposition potential. Figure S13 reveals that a Li<sub>2</sub>O interphase slows the rate of SEI growth by over a factor of 5, compared to a traditional reduced Li<sub>6</sub>PS<sub>5</sub>Cl interphase. It shouldn't therefore come as a surprise that the impedance using lithium metal foil anodes seems to grow less rapidly than in the Li-less configuration,<sup>20</sup> as lithium metal foils have a native passivation layer. Li-less approaches might be more challenging to implement.

## Experimental Procedures

Electrochemistry experiments were performed at a pressure of 13 MPa in an Argon chamber at a temperature of 30 °C using a VMP3 BioLogic potentiostat. All two electrode experiments used 100 mg of Li<sub>6</sub>PS<sub>5</sub>Cl (Ampcera 10 µm) pressed at 370 MPa for 300 s using stainless steel plungers in a Macor cylinder (internal diameter = 10 mm), to yield a pellet of ~700 µm in thickness. Lithium counter electrodes were prepared by cleaning and calendering lithium to 200 µm, cutting out a 10 mm disc and pressing onto the bottom side of a Li<sub>6</sub>PS<sub>5</sub>Cl pellet at 80 MPa for 30 s. Stainless steel working electrodes were prepared by simply placing a stainless steel plunger directly onto the top side of the Li<sub>6</sub>PS<sub>5</sub>Cl pellet inside the Macor cylinder. For three electrode measurements a PEEK cylinder was used in place of the Macor cylinder, that was cut in half perpendicular to the internal 10 mm hole and held together with 3 screws. Between the two pieces of PEEK an InLi alloy ring (internal diameter 10 mm) was placed that was aligned with a stainless steel plunger. A fourth screw was used to make electrical contact to the InLi ring. The cut of the PEEK body was positioned so that the InLi alloy ring was positioned in the middle of a 150 mg Li<sub>6</sub>PS<sub>5</sub>Cl pellet. All other cell assembly steps were identical to two electrode cell assemblies. All cells were left in an environmental chamber for a minimum of 10 hours prior to experiments commencing, to allow for temperature stabilisation.

All voltammetry experiments were conducted at a scan rate of 100 µV s<sup>-1</sup> and a starting potential of 2.2 V vs. Li<sup>+</sup>/Li. Cyclic voltammetry used a first vertex potential of 0.1 V vs. Li<sup>+</sup>/Li and a second vertex potential of 2.2 V vs. Li<sup>+</sup>/Li. CTCA applied a current of -12.25 µA for 6 minutes

during the plating steps. Potentio electrochemical impedance spectroscopy (PEIS) was conducted between frequencies of 400 kHz to 10 Hz with 10 points per decade with a logarithmic spacing with two measurements taken per frequency. A sinus amplitude of 10 mV was used and a 0.1 wait period was used before each frequency and drift correction was used. Impedance spectra were fitted using the inbuilt Z fit function inside EC-lab. A Randles circuit was used, with the Warburg element replaced by an open-circuited uniform distributed resistor constant phase element (URQ) transmission line (Figure S4). All fitting data not shown in the main text can be found in Table S3 and S4 along with Figure S14.

An In+25%Li alloy was used as a reference in 3 electrode cells, due to creep issues when Li rings were tested. The alloy was prepared as follows. Indium (Alfa Aesar 99.99%, lump) and lithium (99.9% Alfa Aesar) were weighed (MTI PCB-200) to make a 75:25 atomic ratio. These were put into a lined (molybdenum foil, Goodfellow) stainless steel crucible. The mixture was heated to 700 °C in a box furnace (MTI KSL-1200X-J-UL) within an argon glovebox. Once molten the crucible was removed from the furnace, stirred with a spatula, and then returned to the furnace for 2 hours, then the crucible was removed and the alloy melt poured onto the stainless-steel glovebox base, such that it rapidly cooled; leading to a fine two-phase microstructure. Physically the cast alloy looked like indium and was soft. Characterisation of the cast two phase alloy is provided in the supplementary information of Aspinall *et al.*<sup>19</sup> The electrochemical potential of this cast alloy was found to be stable within a fraction of a millivolt at 0.622 V vs Li<sup>+</sup>/Li.

The reference ring (Figure 2b insert) minimises impedance artifacts as the SE separator, working electrode and counter electrode all have the same diameter and are aligned to each other in the PEEK housing, whilst the hole in the ring matches the SE separator diameter.<sup>28</sup> The ring design allowed the reference to be directly next to the field lines, yet not impede the flow of Li ions as previous three electrode solid state setups have done.<sup>29–32</sup>

For XPS a 5 mm diameter argyrodite pellet (30 mg) was placed on top of a 4.76 mm diameter Li foil, which was then placed on top of a copper foil. This stack was pressed at ~50 MPa to ensure good contact. The sample stack was grounded to the XPS sample stage using carbon tape. The sample stage was then transferred from the Ar glovebox to the

XPS system (PHI VersaProbe III) using a vacuum transfer vessel (MOD 07-111K, ULVAC-PHI, Inc.) to avoid air contamination. The X-ray source was Al K $\alpha$  ( $h\nu = 1486.8$  eV) and the vacuum level maintained below  $10^{-6}$  Pa throughout this experiment. After collecting the XPS data on the pristine surface, the pellet was exposed to a  $\sim 5$  mm electron beam for 1 hour from an electron neutraliser within the XPS system, driving lithium-ion migration through the pellet. The current of the applied electron beam was set as  $2.5\ \mu\text{A}$ , corresponding to a current density of  $12.74\ \mu\text{A}\ \text{cm}^{-2}$ . After the electron beam, XPS measurements were performed continuously. Each XPS measurement was conducted as follows, a survey scan (pass energy of 224 eV) then high-resolution scans (pass energy of 55 eV) of P 2p, Li 1s, S 2p, O 1s, Cl 2p, and C 1s. Each full sequence of measurements took  $\sim 53$  minutes to complete. All collected data was processed using CasaXPS software<sup>33</sup> and calibrated to the Cl 2p<sub>3/2</sub> peak at 198.5 eV. The standard deviation in the individual P 2p peak areas in Figure 3c was estimated using CasaXPS and used to calculate the uncertainties presented in Figure 3e.

Soft and hard X-ray photoelectron spectroscopy (SOXPES and HAXPES) was performed at the I09 beamline at the Diamond Light Source (Didcot, UK). SOXPES was performed with variable incident X-ray energies, providing emitted photoelectrons with a kinetic energy of 315 eV, while HAXPES was performed with incident X-ray energies of 2.2 and 6.6 keV. This results in electron inelastic-mean-free-paths (IMFPs) of approximately 1, 5 and 14 nm for the SOXPES, 2.2 keV and 6.6 keV photons, respectively (Figure S9). IMFPs were estimated using the TPP-2M formula for both Li<sup>0</sup> and Li<sub>6</sub>PS<sub>5</sub>Cl, giving both upper and lower bounds, respectively. To minimise beam damage the undulator was detuned to provide an X-ray intensity of  $I_0/10$  for HAXPES and  $I_0/100$  for SOXPES, where  $I_0$  is the full beam intensity. The defocussed X-ray beam gave dimensions of 300 (vertical)  $\times$  300 (horizontal) mm and impinged upon the sample surface at an angle of 15° to enhance the photoelectron signal and yield a 300  $\times$  1200 mm illuminated area. The energy distribution curves (EDCs) of the photoelectrons leaving the surface were measured with a concentric hemispherical analyser (VG Scienta EW4000 10 keV, lens acceptance angle  $\pm 28^\circ$ ). The hemispherical analyser was operated with a pass energy of 200 eV for HAXPES and 100 eV for SOXPES. Li<sub>6</sub>PS<sub>5</sub>Cl pellets were prepared as

above and introduced into the end station using an inert transfer vessel. A 20 nm thick film of lithium metal was thermally evaporated onto the Li<sub>6</sub>PS<sub>5</sub>Cl in situ using a custom-built ultrahigh vacuum (UHV) chamber attached to the beamline end station<sup>24</sup> and all samples were stored under UHV throughout the duration of the experiment.

## Acknowledgements

This work was supported by the Faraday Institution SOLBAT and Characterisation projects (grant numbers FIRG056 and FIRG020) and Henry Royce Institute (through UK Engineering and Physical Science Research Council grant EP/R010145/1). M.P. is grateful for the support of Nissan Motor Co. Ltd., Japan. B.J. is grateful for the support of the Clarendon Fund Scholarships. R.S.W. acknowledges a UKRI Future Leaders Fellowship (MR/V024558/1) and funding from the European Research Council (ERC) under the European Union's Horizon 2020 research and innovation programme (EXISTAR, grant agreement No. 950598). We acknowledge Diamond Light Source for synchrotron beamtime on the I09 beamline (SI 25807) and thank the beamline staff for their support. Tien-lin Lee is also acknowledged for helping develop the synchrotron Li deposition setup and helping conduct some SOXPES/HAXPES experiments.

## Supporting Information

### Author contributions

M.B. and M.P. conceived the idea. M.B. performed the all the experiments, with the exception of XPS which was performed by Y.L. whilst J.A. made the InLi alloy. SOXPES and HAXPES measurements were conceived and by J.S.G. and R.S.W. and performed by J.E.S.N., J.S.G. and R.S.W.. Y.L. and B.J. fitted the XPS spectra, and B.J. analyzed the SOXPES and HAXPES data with input from J.S.G. and R.S.W.. M.B. wrote the manuscript with input from all authors. M.P. supervised the design of the project and provided frequent input on the interpretation of all results.

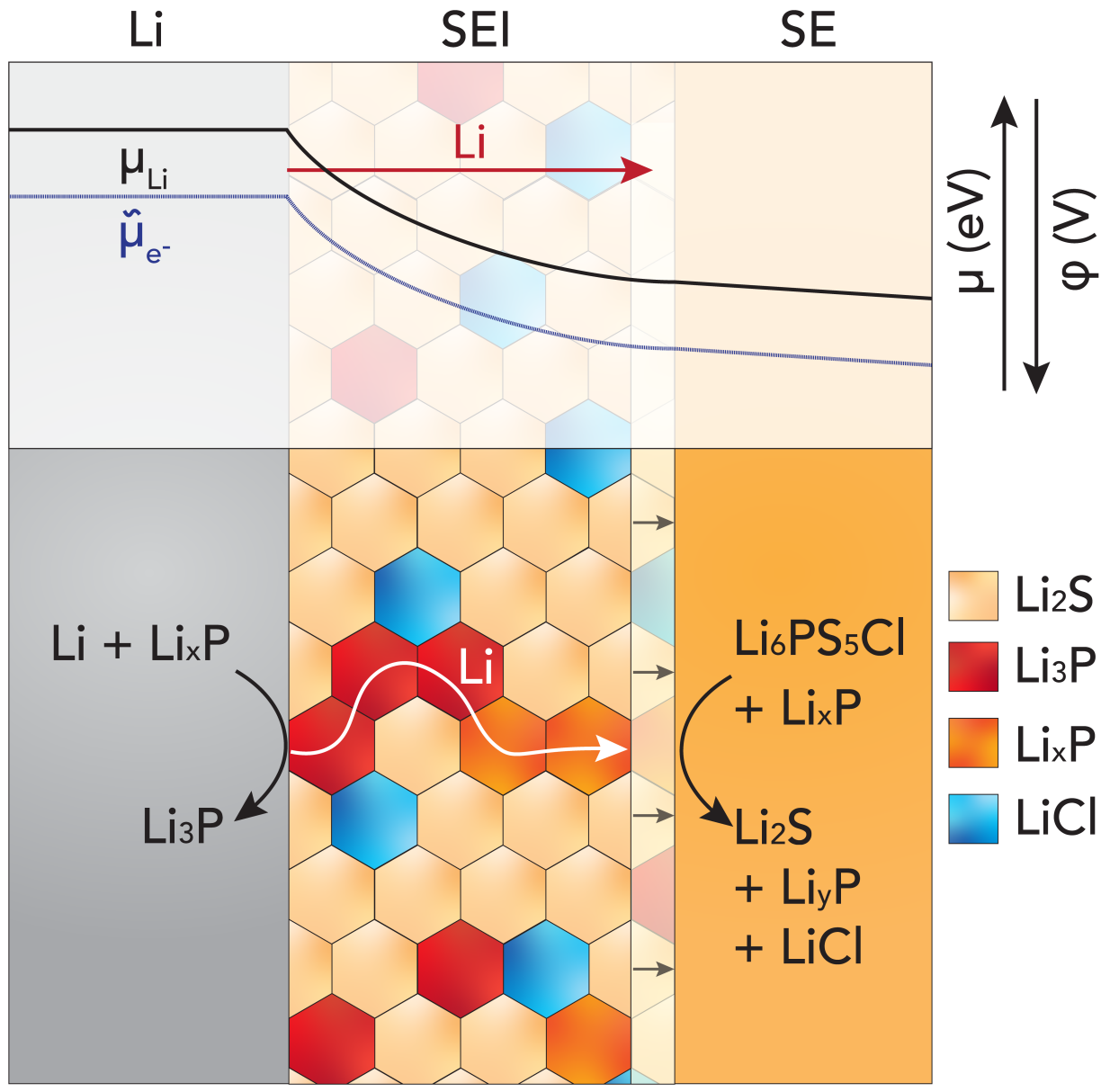
### Declaration of interests

The authors declare no competing interests.

## References

1. Interantional Energy Agency. *Batteries and Secure Energy Transitions* tech. rep. (2024).
2. Zor, C., Turrell, S. J., Uyanik, M. S. & Afyon, S. Lithium Plating and Stripping: Toward Anode-Free Solid-State Batteries. *Advanced Energy and Sustainability Research* **2300001** (2023).
3. Jagger, B. & Pasta, M. Solid electrolyte interphases in lithium metal batteries. *Joule* **7**, 2228–2244 (2023).
4. Schmaltz, T. *et al.* A Roadmap for Solid-State Batteries. *Advanced Energy Materials* **2301886** (2023).
5. Janek, J. & Zeier, W. G. Challenges in speeding up solid-state battery development. *Nature Energy* **8**, 230–240 (2023).
6. Zhu, Y., He, X. & Mo, Y. Origin of Outstanding Stability in the Lithium Solid Electrolyte Materials: Insights from Thermodynamic Analyses Based on First-Principles Calculations. *ACS Applied Materials and Interfaces* **7**, 23685–23693 (2015).
7. Deiseroth, H.-J. *et al.* Li 6 PS 5 X: A Class of Crystalline Li-Rich Solids With an Unusually High Li + Mobility. *Angewandte Chemie* **120**, 767–770 (2008).
8. Wenzel, S., Leichtweiss, T., Krüger, D., Sann, J. & Janek, J. Interphase formation on lithium solid electrolytes - An in situ approach to study interfacial reactions by photoelectron spectroscopy. *Solid State Ionics* **278**, 98–105 (2015).
9. Peled, E. & Menkin, S. Review—SEI: Past, Present and Future. *Journal of The Electrochemical Society* **164**, A1703–A1719 (2017).
10. Wenzel, S. *et al.* Interphase formation and degradation of charge transfer kinetics between a lithium metal anode and highly crystalline Li<sub>7</sub>P<sub>3</sub>S<sub>11</sub> solid electrolyte. *Solid State Ionics* **286**, 24–33 (2016).
11. Otto, S.-K. *et al.* In Situ Investigation of Lithium Metal–Solid Electrolyte Anode Interfaces with ToF-SIMS. *Advanced Materials Interfaces* **9**, 2102387 (2022).
12. Narayanan, S. *et al.* Effect of current density on the solid electrolyte interphase formation at the lithiumLi<sub>6</sub>PS<sub>5</sub>Cl interface. *Nature Communications* **13**, 1–9 (2022).
13. Aktekin, B. *et al.* SEI growth on Lithium metal anodes in solid-state batteries quantified with coulometric titration time analysis. *Nature Communications* **14**, 6946 (2023).
14. Wenzel, S., Sedlmaier, S. J., Dietrich, C., Zeier, W. G. & Janek, J. Interfacial reactivity and interphase growth of argyrodite solid electrolytes at lithium metal electrodes. *Solid State Ionics* **318**, 102–112 (2018).
15. Ning, Z. *et al.* Dendrite initiation and propagation in lithium metal solid-state batteries. *Nature* **618**, 287–293 (2023).
16. Dewald, G. F. *et al.* Experimental assessment of the practical oxidative stability of lithium thiophosphate solid electrolytes. *Chemistry of Materials* **31**, 8328–8337 (2019).
17. Mayo, M., Griffith, K. J., Pickard, C. J. & Morris, A. J. Ab Initio Study of Phosphorus Anodes for Lithium- and Sodium-Ion Batteries. *Chemistry of Materials* **28**, 2011–2021. arXiv: 1510.03248 (2016).
18. Capone, I. *et al.* Electrochemo-Mechanical Properties of Red Phosphorus Anodes in Lithium, Sodium, and Potassium Ion Batteries. *Matter* **3**, 2012–2028 (2020).
19. Aspinall, J. *et al.* Effect of Microstructure on the Cycling Behavior of Li–In Alloy Anodes for Solid-State Batteries. *ACS Energy Letters* **9**, 578–585 (2024).
20. Kasemchainan, J. *et al.* Critical stripping current leads to dendrite formation on plating in lithium anode solid electrolyte cells. *Nature Materials* **18**, 1105–1111 (2019).
21. Schlenker, R. *et al.* Understanding the Lifetime of Battery Cells Based on Solid-State Li<sub>6</sub>PS<sub>5</sub>Cl Electrolyte Paired with Lithium Metal Electrode. *ACS Applied Materials and Interfaces* **12**, 20012–20025 (2020).
22. Siroma, Z. *et al.* Mathematical solutions of comprehensive variations of a transmission-line model of the theoretical impedance of porous electrodes. *Electrochimica Acta* **160**, 313–322 (2015).

23. Alt, C. D. *et al.* Quantifying multiphase SEI growth in sulfide solid electrolytes. *Joule*, 1–22 (2024).
24. Gibson, J. S. *et al.* Gently does it!: in situ preparation of alkali metal-solid electrolyte interfaces for photoelectron spectroscopy. *Faraday Discuss.* **236**, 267–287 (2022).
25. Yeh, J. J. & Lindau, I. Atomic subshell photoionization cross sections and asymmetry parameters:  $1 \leq Z \leq 103$ . *At. Data Nucl. Data Tables* **32**, 1–155 (1985).
26. Ren, F. *et al.* Visualizing the SEI formation between lithium metal and solid-state electrolyte. *Energy Environmental Science* **17**, 2743–2752 (2024).
27. Randau, S. *et al.* Benchmarking the performance of all-solid-state lithium batteries. *Nature Energy* **5**, 259–270 (2020).
28. Ender, M., Illig, J. & Ivers-Tiffée, E. Three-Electrode Setups for Lithium-Ion Batteries. *Journal of The Electrochemical Society* **164**, A71–A79 (2017).
29. Riegger, L. M. *et al.* Evolution of the Interphase between Argyrodite-Based Solid Electrolytes and the Lithium Metal AnodeThe Kinetics of Solid Electrolyte Interphase Growth. *Chemistry of Materials* **35**, 5091–5099 (2023).
30. Hertle, J. *et al.* Miniaturization of Reference Electrodes for Solid-State Lithium-Ion Batteries. *Journal of The Electrochemical Society* **170**, 040519 (2023).
31. Chang, G. H., Choi, H. U., Kang, S., Park, J. Y. & Lim, H. T. Characterization of limiting factors of an all-solid-state Li-ion battery using an embedded indium reference electrode. *Ionics* **26**, 1555–1561 (2020).
32. Ikezawa, A. *et al.* Performance of Li<sub>4</sub>Ti<sub>5</sub>O<sub>12</sub>-based reference electrode for the electrochemical analysis of all-solid-state lithium-ion batteries. *Electrochemistry Communications* **116**, 106743 (2020).
33. Fairley, N. *et al.* Systematic and Collaborative Approach to Problem Solving Using X-ray Photoelectron Spectroscopy. *Appl. Surf. Sci. Adv.* **5**, 100112 (2021).



Graphical Abstract